Geotechnical Site Characterization with 3D Ambient Noise Tomography: Field Data Applications

Yao Wang[1]; Khiem T. Tran, Ph.D.[2]; Brady Cox[3]; and Joseph P. Vantassel[4]

[1]Ph.D. Student, Dept. of Civil and Coastal Engineering, Univ. of Florida, Gainesville, FL.
Email: wangyao@ufl.edu
[2]Associate Professor, Dept. of Civil and Coastal Engineering, Univ. of Florida, Gainesville, FL.
Email: ttk@ufl.edu
[3]Professor, Dept. of Civil and Environmental Engineering, Utah State Univ., Logan, UT.
Email: brady.cox@usu.edu
[4]Research Associate, Texas Advanced Computing Center, Austin, TX.
Email: jvantassel@utexas.edu

ABSTRACT

A new 3D ambient noise tomography (3D ANT) method is presented for geotechnical site characterization. It requires recording ambient noise wavefields using a 2D surface array of geophones, from which cross-correlation functions (CCF) are then extracted and directly inverted to obtain S-wave velocity (Vs) structure. The method consists of a forward simulation using 3D P-SV elastic wave equations to compute the synthetic CCF and an adjoint-state inversion to match synthetic and field CCFs for extraction of Vs. Compared to conventional passive seismic methods using characteristics of Green's function (GF), the main advantage of the presented method is that it does not require the energy balance at both sides of each receiver pair to retrieve the true GF. Instead, the source power spectrum density is inverted during the analysis and incorporated into the forward simulation to account for source energy distribution for accurate extraction of Vs profiles. The presented 3D ANT method was applied to 3 h of noise recordings from an array of 196 geophones placed on a grid with 5 m spacing at the Garner Valley Downhole Array (GVDA) site in California. The inverted 3D Vs model is found to be consistent with previous invasive and non-invasive geotechnical characterization efforts at the GVDA site.

INTRODUCTION

Active-source seismic methods such as multichannel analysis of surface waves (MASW) and full-waveform inversion (FWI) have become efficient tools for geotechnical site characterization. While these methods can provide accurate subsurface profiles, they require low-frequency energy (<10 Hz) for deep investigation (> 20 m in depth). As large, powerful active sources capable of generating such low-frequency energy are expensive and generally not available for use on most projects, many have sought to take advantage of the low-frequency ambient noise already present in the environment for deep site characterization.

Besides the conventional anbient noise methods based on dispersion characteristics, full-waveform inversion (FWI) of cross-correlation functions (CCF) of noise fields have been recently studied. Toward the FWI of CCFs, structural and source kernels were first derived by Tromp et al. (2010). The practical field applications have been conducted at global and local scales (De Ridder and Maddison, 2018; Sager et al., 2018). At engineering scales (< 50 m depth), the 2D ambient noise tomography (2D ANT; Wang et al., 2021) has recently been developed.

This method uses traffic noise fields with known wave propagation direction (along roadway). The 2D ANT was able to invert CCFs of the traffic noises to extract 2D Vs profiles to detect roadway sinkholes. Building on our success of the 2D ANT, this study developed a new 3D ANT method to directly invert CCFs of ambient noise fields for extraction of subsurface 3D Vs profiles. The main advantage of inverting CCFs is that it does not rely on Green's function retrieval. Therefore, it doesn't require the energy balance at both sides of each receiver pair to retrieve the true GFs. Instead, the source power spectrum density is inverted during the analysis and incorporated into the forward simulation to account for source energy distribution for accurate extraction of Vs profiles. The 3D ANT method's capabilities are evaluated with field noise data.

METHODOLOGY

The presented 3D ANT method consists of a forward simulation to compute the cross-correlation function (CCF) and an adjoint-state inversion to match simulated and observed CCFs for extraction of subsurface structures. 3D P-SV elastic wave equations and their numerical solutions (Nguyen and Tran, 2018) are used to simulate noise fields and Green's functions required for computing the CCF during inversion, as discussed in the following sections.

Forward simulation

The CCF $C^{\alpha\beta}$ between the two signals s^{α} and s^{β} is explicitly given by:

$$C^{\alpha\beta}(t) = \int s^{\alpha}(\tau) s^{\beta}(t+\tau) d\tau. \tag{1}$$

Variables α and β are indexing the receiver stations. Equation (1) requires performing the forward simulation for each source location individually to obtain seismograms $s^{\alpha}$and s^{β}. However, it is not practical to explicitly simulate the seismograms due to a large number of sources with unknown locations. Thus, we adopt the implicit approach (Sager et al., 2018, 2020; Wang et al., 2021) to compute the CCF. The CCF can be formulated via Green's functions as:

$$C^{\alpha\beta}(t) = \frac{1}{2\pi} \int \int_{\Omega''} \int_{\Omega'} \mathrm{G}(\boldsymbol{x}^{\alpha}, \boldsymbol{x}', \omega)\, \mathrm{f}(\boldsymbol{x}', \omega)\, \mathrm{G}^{*}\left(\boldsymbol{x}^{\beta}, \boldsymbol{x}'', \omega\right) \mathrm{f}^{*}(\boldsymbol{x}'', \omega) \exp(i\omega t)\, d\Omega' \mathrm{d}\Omega''\, d\omega. \tag{2}$$

In this equation, $\boldsymbol{x}'$ and $\boldsymbol{x}''$ are two arbitrary locations in the 3-D domain Ω. Integrals $\int_{\Omega'} d\Omega'$ and $\int_{\Omega''} d\Omega''$ denote the integration over domain Ω twice, distinctively. $\mathrm{G}(\mathbf{x}^{\alpha}, \mathbf{x}, \mathrm{t})$ is the Green's function with the source located at $\mathbf{x}^{\alpha}$, and $\mathrm{f}(\mathbf{x}, \mathrm{t})$ is the source function. Assuming that the spatial correlation length of noise sources is shorter than seismic wavelengths, the source terms can be approximated with a delta function in space and the source power spectrum density (PSD) $S(\boldsymbol{x}, \omega)$ (Wapenaar, 2004; Wapenaar and Fokkema, 2006):

$$\mathrm{f}(\boldsymbol{x}', \omega)\, \mathrm{f}^{*}(\boldsymbol{x}'', \omega) = S(\boldsymbol{x}', \omega) \delta(\boldsymbol{x}' - \boldsymbol{x}''), \tag{3}$$

By its definition, the PSD is a field of scalar values that show the spatial location and the strength of sources. With this approximation, equation 2 becomes:

$$C^{\alpha\beta}(t) = \frac{1}{2\pi}\int\int_{\Omega} G(\mathbf{x}^{\alpha}, \mathbf{x}, \omega)\left[G^{*}\left(\mathbf{x}^{\beta}, \mathbf{x}, \omega\right) S(\mathbf{x}, \omega)\right] \exp(i\omega t)\, d\mathbf{x} d\omega, \quad (4)$$

and

$$C^{\alpha\beta}(\omega) = \int_{\Omega} G(\mathbf{x}^{\alpha}, \mathbf{x}, \omega)\left[G^{*}\left(\mathbf{x}^{\beta}, \mathbf{x}, \omega\right) S(\mathbf{x}, \omega)\right] d\mathbf{x}. \quad (5)$$

Equations (4) and (5) compute the CCF in the time and the frequency domain, respectively. Using equation (5), the CCF is computed implicitly for a given noise source distribution (all noise events) instead of individual noise events. We compute the CCF between $\mathbf{x}^{\alpha}$ and $\mathbf{x}^{\beta}$ by performing the following steps:

1) Run two forward simulations to compute Green's functions $G(\mathbf{x}^{\alpha}, \mathbf{x}, \omega)$ and $G\left(\mathbf{x}^{\beta}, \mathbf{x}, \omega\right)$ with sources at $\mathbf{x}^{\alpha}$ and $\mathbf{x}^{\beta}$.
2) Multiply $G(\mathbf{x}^{\alpha}, \mathbf{x}, \omega)$ with the complex conjugate $G^{*}(\mathbf{x}^{\beta}, \mathbf{x}, \omega)$ and the noise source PSD $S(\mathbf{x}, \omega)$.
3) Sum over all grid points (integration over space $\mathbf{x}$), and 4) transform the frequency-domain CCF to the time domain. In this study, the PSD is inverted from measured CCFs, and $S(\mathbf{x},\omega)$ is the same (average value) for all frequencies within a filtering band.

Adjoint-state inversion

The inversion process minimizes the misfit between the observed and the simulated CCFs to extract the subsurface velocity structures. We define the misfit (residual) between the observed and synthetic CCFs as:

$$\delta C = C_{obs} - C_{syn}. \quad (6)$$

The objective function is then defined as the L2-norm of the misfit:

$$E = \frac{1}{2}\delta C^{T}\delta C = \frac{1}{2}\sum_{\alpha}\int dt \sum_{\beta} \delta C^{2}. \quad (7)$$

To optimize the objective function, we analyze the three main components that produce the misfit of CCFs. They are the source signature (source time function), the source power spectrum density (PSD), the geologic structure (Vs, Vp, and density). The source signature governs the shape of the CCF waveforms, the PSD defines the location and strength of the noise sources, and the geologic structure influences the wave propagation. Among these three components, the source time function estimation is relatively straightforward because it could be implemented in the data domain without using a geologic model. The source time function is estimated from the ambient noise records using a deconvolution method (Wang et al., 2021). This method is applied to all examples for source signal estimation throughout this work. To address the remaining two components, we invert the PSD and Vs using their sensitive kernels developed by Sager et al., 2020.

To update the spatial component of the power spectral density distribution, we use the adjoint techniques to calculate the PSD kernel (Sager et al., 2020):

$$K_s(x) = -\sum_{\alpha=1}^{n} \int u^{\dagger}(\boldsymbol{x})[G^*(\alpha, x)S(x)]d\omega. \quad (8)$$

The calculation of this kernel consists of two wavefield simulations. $u^{\dagger}$ is the adjoint wavefield and $G^*(\alpha, x)S(x)$ is the broadcast wavefield of the forward-propagating wavefield recorded at any area where the PSD is positive (where a source exists). The frequency-domain multiplication is implemented by a time-domain convolution (zero-lag cross-correlation).

Next, the geologic structure refers to an Earth model $\boldsymbol{m}(\boldsymbol{x})$, which characterizes the subsurface material properties (V_p, V_s, ρ). The vector $\boldsymbol{m}(\boldsymbol{x})$ controls Green's functions in the forward simulation equations (4) and (5). To derive the kernel, we use the elastic wavefield modeling operator as $\mathcal{L}(\circ)$, where $\circ$ is a place holder. With this operator, $\mathcal{L}(u(x))$ represents the forward elastic wavefield simulation in terms of displacement vector $\boldsymbol{u}(\boldsymbol{x})$. The time-domain finite-difference implementation of $\mathcal{L}(\circ)$ (Nguyen and Tran, 2018) is used for wavefield simulation throughout this work. The structural kernel with respect to $\boldsymbol{m}(\boldsymbol{x})$ is computed as (Sager et al., 2020):

$$K_m(x) = \sum_{\alpha=1}^{n} \int \left[u^{\dagger}(\boldsymbol{x})\mathcal{L}\big(C(\boldsymbol{x}, \alpha)\big) + C_{\alpha}^{\dagger}(\boldsymbol{x})\mathcal{L}\big(G(\boldsymbol{x}, \alpha)\big)\right]dt\,. \quad (9)$$

For the first part inside the square bracket, the adjoint wavefield $u^{\dagger}(\boldsymbol{x})$ is numerically computed by injecting the CCF residuals (equation 6) at the receiver locations. At each reference station α, the residual δC_{α} consists of n channels, which are backward propagated simultaneously to generate wavefield $u^{\dagger}$. The operation $\mathcal{L}\big(C(\boldsymbol{x}, \alpha)\big)$ denotes the correlation wavefield propagates from the noise source to the receivers. To calculate this wavefield, we first inject the source time function at the reference station α and record the forward-propagating wavefield at any area where there is a noise source (with a PSD magnitude >0). We then do another forward simulation to broadcast the recorded wavefield and multiply the broadcast wavefield with the PSD to produce the wavefield $\mathcal{L}\big(C(\boldsymbol{x}, \alpha)\big)$.

For the second part inside the square bracket, $C_{\alpha}^{\dagger}$ denotes the adjoint CCF residual wavefield. It is calculated by:

$$C_{\alpha}^{\dagger}(x) = \int G_{\alpha}^{*}(x, t)[u^{\dagger *}(x)S(x)]dt. \quad (10)$$

To compute this wavefield, we perform a forward simulation to backward propagate the CCF residuals δC and record the wavefield at any area with a noise source (PSD>0). Then we do another forward simulation to broadcast the recorded CCF residual wavefield, and multiply the broadcast wavefield with the PSD to obtain wavefield $C_{\alpha}^{\dagger}(x)$. The computing of $\mathcal{L}\big(G(\boldsymbol{x}, \alpha)\big)$ is done by injecting the source time function at station α and recording the forward-propagating wavefield. Similar to the first part in the square bracket, the second part is calculated by performing time-domain convolution of $C_{\alpha}^{\dagger}(x)$ and $\mathcal{L}\big(G(\boldsymbol{x}, \alpha)\big)$.

More specifically, we formulate and compute the gradients for Lamé parameters λ, μ using strains of the simulated wavefields as:

$$\begin{aligned}\delta\lambda = \int_0^T \{&\left(\varepsilon_x + \varepsilon_y + \varepsilon_z\right)\left(\varepsilon_x^{c+} + \varepsilon_y^{c+} + \varepsilon_z^{c+}\right) \\ &+ \left(\varepsilon_x^{+} + \varepsilon_y^{+} + \varepsilon_z^{+}\right)\left(\varepsilon_x^{c} + \varepsilon_y^{c} + \varepsilon_z^{c}\right)\}dt, \\ \delta\mu = \int_0^T \{&\left(\varepsilon_x\varepsilon_x^{c+} + \varepsilon_y\varepsilon_y^{c+} + \varepsilon_z\varepsilon_z^{c+}\right) + \left(\varepsilon_{xy} + \varepsilon_{yx}\right)\left(\varepsilon_{xy}^{c+} + \varepsilon_{yx}^{c+}\right) \\ &+ \left(\varepsilon_{yz} + \varepsilon_{zy}\right)\left(\varepsilon_{yz}^{c+} + \varepsilon_{zy}^{c+}\right) + \left(\varepsilon_{zx} + \varepsilon_{xz}\right)\left(\varepsilon_{zx}^{c+} + \varepsilon_{xz}^{c+}\right) \\ &+ \left(\varepsilon_x^{c}\varepsilon_x^{+} + \varepsilon_y^{c}\varepsilon_y^{+} + \varepsilon_z^{c}\varepsilon_z^{+}\right) + \left(\varepsilon_{xy}^{c} + \varepsilon_{yx}^{c}\right)\left(\varepsilon_{xy}^{+} + \varepsilon_{yx}^{+}\right) \\ &+ \left(\varepsilon_{yz}^{c} + \varepsilon_{zy}^{c}\right)\left(\varepsilon_{yz}^{+} + \varepsilon_{zy}^{+}\right) + \left(\varepsilon_{zx}^{c} + \varepsilon_{xz}^{c}\right)\left(\varepsilon_{zx}^{+} + \varepsilon_{xz}^{+}\right)\} dt.\end{aligned} \tag{11}$$

The strain tensor $\boldsymbol{\varepsilon}$ is computed via the particle displacement $\boldsymbol{u}$ as $\boldsymbol{\varepsilon}_{ij} = \frac{1}{2}\left(\frac{\partial \boldsymbol{u}_i}{\partial x_j} + \frac{\partial \boldsymbol{u}_j}{\partial x_i}\right)$. Notation ε is the strain of the forward-propagating wavefield $\mathcal{L}\left(G(\boldsymbol{x},\alpha)\right)$, ε^{+} is the strain of the adjoint wavefields $u^{\dagger}$, ε^{c} is the strain of the propagating of correlation wavefields $\mathcal{L}\left(C(\boldsymbol{x},\alpha)\right)$, and ε^{c+} is the strain of the adjoint correlation wavefield $C^{\dagger}$. Based on the relationships between variables Vs, λ, μ, and density ρ, the gradient with respect to Vs can be written as:

$$\delta \mathrm{Vs} = -4\rho \mathrm{Vs}\delta\lambda + 2\rho \mathrm{Vs}\delta\mu. \tag{12}$$

Finally, the PSD and Vs are updated iteratively by

$$\begin{cases} S^{p+1} = \|S^{p} + \theta_1 |K_s|_{L1}\|, \\ \mathrm{V_s^{p+1}} = \mathrm{V_s^{p}} + \theta_2 \delta \mathrm{V_s}. \end{cases} \tag{13}$$

The index p denotes the iteration number. The operator $|\circ|_{L1}$ is the L-1 normalization. The operator $\|\circ\|$ denotes a PSD magnitude normalization. This normalization neglects the negative values and maps the non-negative magnitude of the PSD to the range [0,1]. The step length θ_1 and θ_2 are positive scalers. The gradient δV_s is normalized by dividing its maximum magnitude. In this study, we use θ_1 equal to 0.05 (5% of the maximum normalized PSD) and θ_2 equal to 0.02 (2% of the maximum Vs) of the current model during inversion.

FIELD EXPERIMENT

A field experiment was conducted at the Garner Valley Downhole Array (GVDA) test site (Figure 1), in California. The site is located in a seismically active region of southern California, approximately 115 km northeast of San Diego, 150 km southeast of Los Angeles, 7 km east of the San Jacinto Fault, and 35 km west of the San Andreas Fault (Teague et al., 2018). More information about this site can be obtained at http://nees.ucsb.edu/facilities/GVDA. Invasive and non-invasive geotechnical site charachterization efforts performed previously at the GVDA site include: downhole seismic testing, P-S suspension logging (Stellar 1996), MASW and microtremor array measurements (MAM) (Teague et al., 2018), and active-source FWI (Fathi et al., 2016). These investigations indicated that this site comprises 18-25 m of mostly sandy- to silty-sand alluvium (AL), overlaying decomposed granite (DG) that eventually transitions into unweathered granite at depths that vary between about 60 – 90 m across the site. The exact locations for some of these previous seismic tests are displayed in Figure 1 relative to a large 2D sensor array used to collect data for this study.

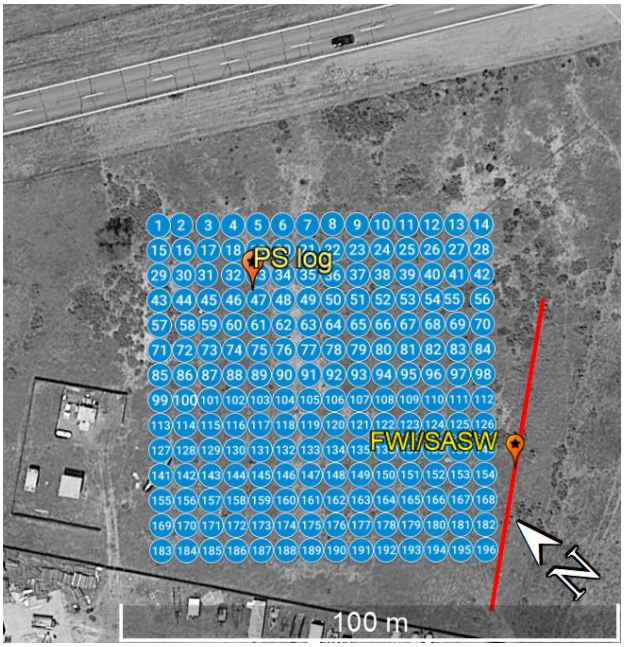

Figure 1. Plan view of the GVDA test site with the locations of several seismic testing boreholes and sensor arrays indicated. The blue circles represent the 196, 3-component, 5-Hz nodal staions used for 3D ANT in the present study, which were deployed in a 14 x 14 grid at a uniform spacing of 5 m.

We deployed an array of 196, 3-component, 5-Hz nodal sensors on a 14 × 14 grid with 5-m uniform spacing on the ground surface at GVDA. We recorded about 28 hours of ambient noises over two night-time deployments. The array's center (33.669°N, 116.673°W) is approximately 60 m to the southwest of a rural highway (the Pines to Palms highway). A ten-second example record of the recorded noise data is displayed in Figure 2a. In this plot, seismograms are shown in the offset-time style. The offset is defined by the distance to reference station #1. A traffic-induced surface wave event can be identified from this plot between 3 s and 4 s. This event traveled through the receiver area and left a trace of linear appearance in the seismogram.

The noise data CCF is computed and inverted following the same steps as those of the synthetic example. The entire 28-hour recording is filtered through 2-15 Hz bandwidth, and divided into one-second segments. The CCF between every station pair is calculated for each segment and sum over all segments. The CCFs for between individual stations and reference station #1 are shown in Figure 2b. Consistent wavefroms are observed for most of receiver pairs and clear arrivals can be identified for reference station 1, which it is the closest to the highway (Figure 1).

For the inversion analysis, the velocity model is set as 160 m × 160 m × 45 m (X × Y × Z) and discretized into cells of 2.5 m × 2.5 m × 2.5 m. The receiver patch is near the model's center with the receiver X-locations from 45 m to 110 m, and the receiver Y-locations from 35 m to 100 m (Figure 3). This setting allows the modeled area covering over 100 m length of the highway close to the site, benefiting the noise source distribution estimation. Consulting the SASW result at the site (Fathi et al. 2016), we used a basic 1D initial model with Vs linearly increased from 175 m/s on the ground surface to 500 m/s at the model bottom (50 m depth). The inversion was run for a total of 45 iterations. The inversion alternated between updating the PSD for 5

iterations and upadating the models Vs model for 10 iterations. During inversion, Vp was updated as twice the value of Vs, and ρ was fixed to 1,800 kg/m^3.

Figure 3 shows the inverted normalized PSD with a truncated (0~0.5) color scale used for better showing the traffic noise directions. This result indicates that ambient noise signal arrive from all directions, but mainly from the highway to the north. The signal power is especially strong along the shortest path from the road to the receiver array (Figure 2), indicating that traffic-induced surface waves dominate the recorded noise wavefield and the computed PSD is consistent with the noise sources.

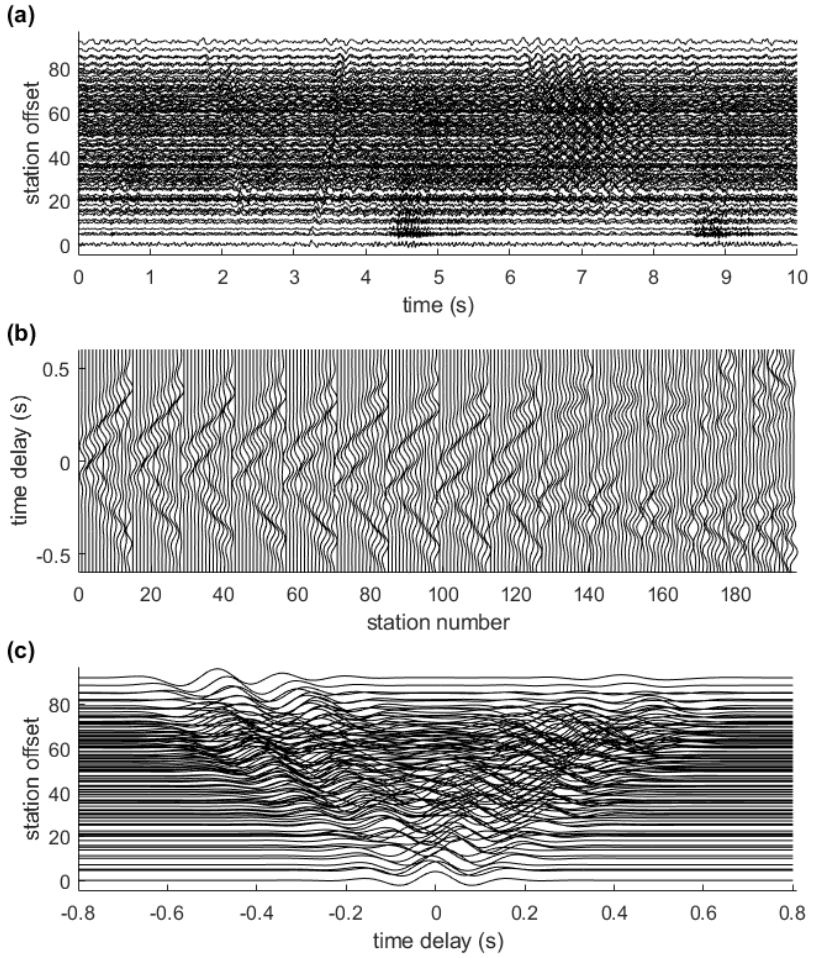

Figure 2. Examples of raw noise data collected at GVDA and experimental CCFs calculated relative to station #1. (a) A ten-second noise record example. (b) The CCF displayed in time-sensor-number style, and (c) offset-time style

The inverted 3D Vs model is displayed in Figure 4. It shows softer materials with Vs < ~250 m/s over the top 10-20 m, which agrees quite well with the expected AL-DG interface, with rapidly increasing Vs at greater depths. The lateral variation of Vs is minimal, although the thickness of the softest, near-surface material does vary signifcantly across the array. Due to the distribution of sensors and the PSD, the characterized area is mainly within the sensor array

(45~110 m in the X-direction and 35~100 m in Y-direction). The initial model was updated very little outside of the sensor array.

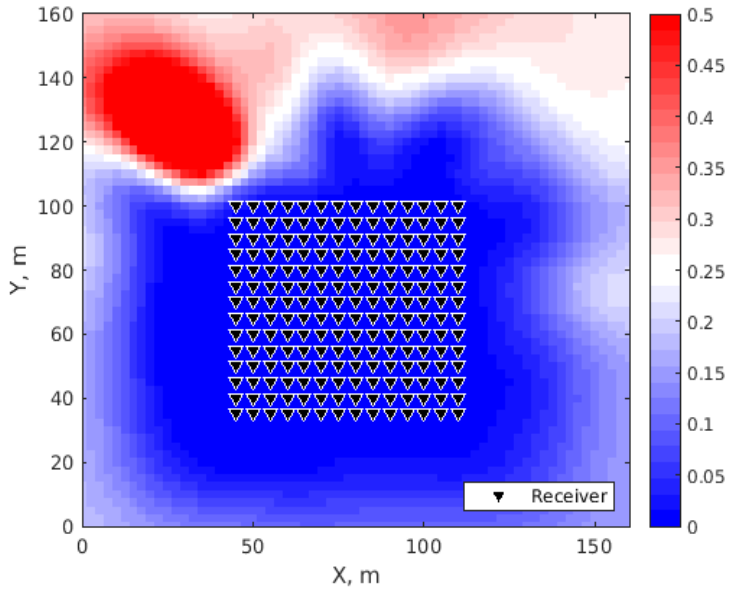

Figure 3. Inverted PSD for the GVDA dataset. The black triangles represent the geophones.

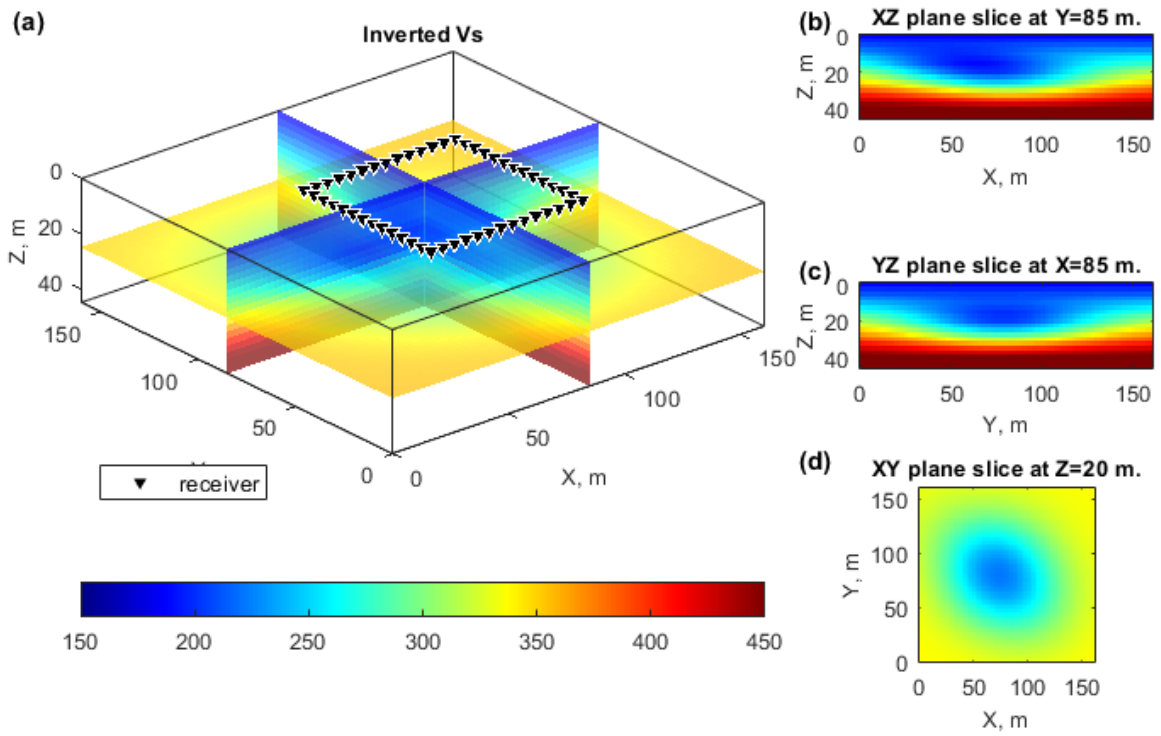

Figure 4. Inverted 3D Vs model for the GVDA dataset. (a) The final inverted Vs model. Black triangles represent receivers on the boundary of the sensor patch. (b) XZ plane slice at Y=85 m. (c) YZ plane slice at X=85 m. (d) XY plane slice at Z=20 m.

To evaluate the 3D ANT algorithm's performance, we compare waveforms of the observed and simulated CCFs. The comparison is carried out using station # 61 as a reference, which is located near the boring log. At this station, the largest station offset is about 65 m (i.e., the distance to station 196). At the first iteration (Figure 5a), there is an evident gap of arrival-times between the observed and simulated CCFs. This difference in arrival-times indicates that the field subsurface has an S-wave velocity slower than the initial model. This time difference is less evident with small station offsets (less than 30 m), implying that the initial model is more accurate in the shallow depths. At the final iteration, the waveform match is considerably improved, and the arrival-time difference is small between the observed and simulated CCFs (Figure 5b). The waveform misfit still exists after the final iteration, mostly due to: (1) the random noise in the recorded data, (2) the error of source signal estimation, (3) the error of PSD estimation, and (4) the error of Vs update. Nevertheless, the inverted Vs model produces much better waveform matches than the initial model, and thus better represents the actual site conditions.

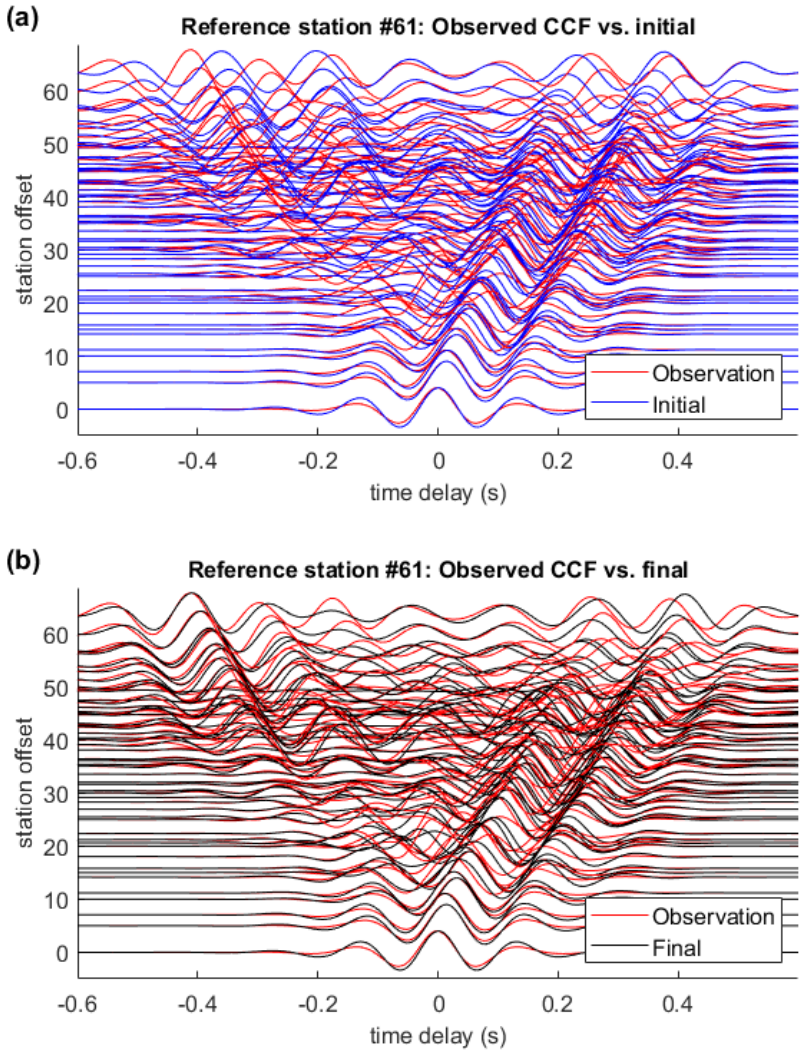

Figure 5. CCF waveform comparisons for the GVDA dataset relative to station 61 after: (a) the first inversion iteration, and (b) the last inversion iteration.

As noted above, Stellar (1996) performed P-S suspension logging (PS logging) at the GVDA site near station # 47 (X=65 m, Y=85 m; refer to Figure 1). To compare the proposed 3D ANT method to ground truth, we compare the initial Vs model, the inverted Vs model, and the simplified PS log data at the borehole's location (Figure 6a). The inverted Vs has good alignment with the PS logging data above 15 m, and correctly reflects the increasing trend of Vs with depth. The AL-DG interface is estimated around 20 m in the 3D ANT result, which is slightly deeper than that from the borehole PS logging data. This is likely due to the smoothness of the 3D ANT result and the resulting lack of reflected waves at the layer interface. Nevertheless, it shows the correct trend of velocity increment with depth.

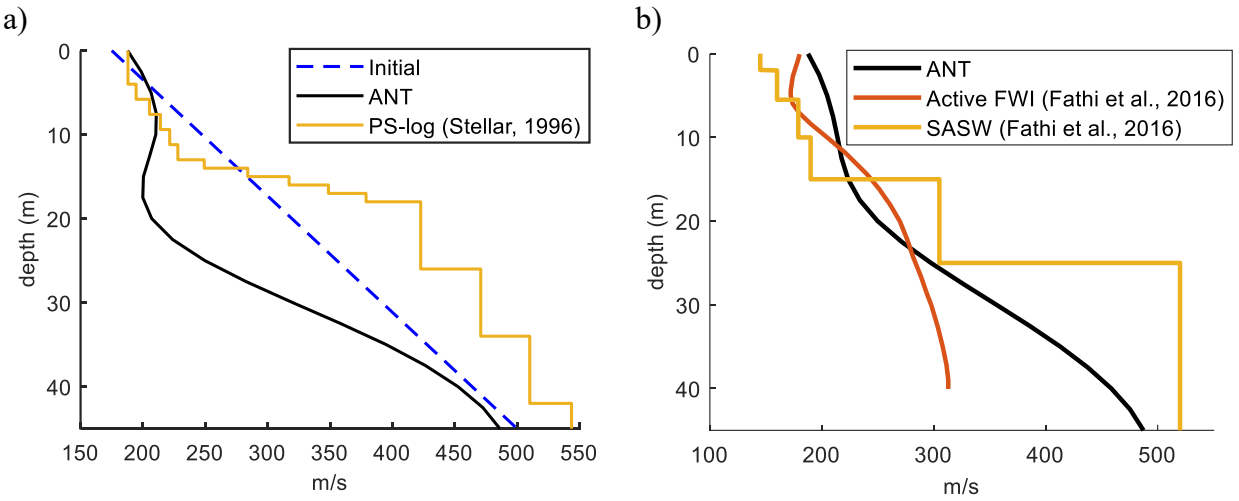

Figure 6. Compariosn of 1D Vs profiles from the present 3D ANT inversion and those obtained previously at the GVDA site: (a) 3D ANT Vs profile from station # 47 at X=65 m, Y=85 m in comparison to the PS logging Vs profile in a nearby borehole. (b) 3D ANT Vs profile from station # 154 at X=110 m, Y=50 m in comparison to nearby SASW and active FWI Vs profiles.

Fathi et al. (2016) performed SASW and active-source FWI at this site. Figure 6b shows the comparison of 1D Vs profiles from the 3D ANT at a point near station #154 (X=110 m, Y=50 m; refer to Figure 1) to those of SASW (line 1) and active FWI (at X = 0 m in Figure 15 of Fathi et al, 2016). The active FWI study provides accurate Vs profiles that agree with the SASW at depths above 10 m. However, the active FWI does not characterize a stiffer layer below 20-m depth, mostly likely due to the lack of low frequency signals (2-5 Hz) used in the analysis. In contrast, the ANT inverted profile is more consistent with the SASW and PS logging results. The ANT and SASW produce similar results because both method utilize the low-frequency components (2-10 Hz) to image the deeper structure.

CONCLUSIONS

This paper presents a new 3D ambient noise tomography (3D ANT) method, which analyzes noise cross-correlation functions (CCF) for characterization of 3D Vs subsuface structure. The novelty of the presented method is that it does not rely on Green's function retrieval, or require the noise wavefield to be far-field. Instead, by accounting for noise source distribution directly, it

inverts the full-waveform CCF for Vs structures. The method's capability is tested on a massive traffic-induced noise dataset collected at Garner Valley Downhole Array (GVDA) test site in southern California. The inverted noise source distribution is consistent with the known ambient sources (a nearby highway) and the inverted Vs model is consistent with prior invasive and non-invasive geotechnical site characterization data. Based on the synthetic and field experimental results, the ANT method is a useful geophysical tool for characterization of 3D soil and rock profile.

ACKNOWLEDGMENTS

This study was financially supported by the National Science Foundation: grants CMMI-1930697 and CMMI-1931162. The supports are greatly appreciated.

REFERENCES

De Ridder, S. A. L., and J. R. Maddison. 2018. Full wavefield inversion of ambient seismic noise: *Geophysical Journal International*, 215, 1215–1230.

Fathi, A., B. Poursartip, K. H. Stokoe II, and L. F. Kallivokas. 2016. Three-dimensional P-and S-wave velocity profiling of geotechnical sites using full-waveform inversion driven by field data: *Soil Dynamics and Earthquake Engineering*, 87, 63–81.

Nguyen, T. D., and K. T. Tran. 2018. Site characterization with 3D elastic full-waveform tomography: *Geophysics*, 83, R389–R400.

Sager, K., L. Ermert, C. Boehm, and A. Fichtner. 2018. Towards full waveform ambient noise inversion: *Geophysical Journal International*, 212, 566–590.

Sager, K., C. Boehm, L. Ermert, L. Krischer, and A. Fichtner. 2020. Global-scale full-waveform ambient noise inversion: *Journal of Geophysical Research: Solid Earth*, 125, e2019JB018644.

Steller, R. "New borehole geophysical results at GVDA," UCSB Internal report; 1996.

Teague, D. P., B. R. Cox, and E. M. Rathje. 2018. Measured vs. predicted site response at the Garner Valley Downhole Array considering shear wave velocity uncertainty from borehole and surface wave methods: *Soil Dynamics and Earthquake Engineering*, 113, 339–355.

Tromp, J., Y. Luo, S. Hanasoge, and D. Peter. 2010. Noise cross-correlation sensitivity kernels: *Geophysical Journal International*, 183, 791–819.

Wang, Y., K. T. Tran, and D. Horhota. 2021. Road sinkhole detection with 2D ambient noise tomography: *Geophysics*, 86, KS123–KS135.

Wapenaar, K. 2004. Retrieving the elastodynamic Green's function of an arbitrary inhomogeneous medium by cross correlation: *Physical Review Letters*, 93, 254301.

Wapenaar, K., and J. Fokkema. 2006. Green's function representations for seismic interferometry: *Geophysics*, 71, SI33–SI46.